551.515.5:551.558.1

Convection in the tropics

By ALAN K. BETTS*

Department of Atmospheric Science, Colorado State University, Fort Collins, Colorado 80523

SUMMARY

The convective organization and budgets for one day during GATE (2 September 1974) are first discussed. A series of models for tropical squall line structure, downdraught thermodynamics, the budget analysis method, trade cumulus, stratocumulus and subcloud layer convection are in turn presented. Tephigram representations are used to represent thermodynamic properties and show similarities and differences.

1. INTRODUCTION

The GARP Atlantic Tropical Experiment (GATE) had two main objectives: the first has been to provide a description of convective organization and transports embedded within the meteorological fields and the second to test and develop conceptual models suitable for the parameterization of convective transports within numerical models. Of its predecessors, the Venezuelan International Meteorological and Hydrological Experiment (VIMHEX) had similar though more modest objectives, and the Barbados Oceanographic and Meteorological Experiment (BOMEX) addressed primarily air–sea interaction as well as the structure of tropical disturbances.

An earlier review (Betts 1974) discussed the scientific objectives of the Convection Subprogramme of GATE: the concept of scale interaction and the problem of parameterization of convection organized on the mesoscale in terms of larger-scale fields. The GATE field experiment has now given us a rather detailed description of the synoptic, mesoscale and convective organization in the eastern Atlantic. One control on the development of cloud clusters (aggregates of mesoscale convective bands) by large-scale waves in the dominant easterly tropospheric flow has been established (Reed *et al.* 1977; Norquist *et al.* 1977) and is discussed here by Reed. The exact role of the mesoscale organization of convection in the parameterization problem is, however, a little clearer now than before GATE. There are both descriptive and theoretical reasons for this which we shall touch on in this paper.

Our understanding of cloud-scale circulations and of the importance of downdraughts has advanced considerably in the last few years. The mass transports local to the clouds may be considerably larger than the mean transport, and cannot be ignored in the analysis and modelling of the disturbed boundary layer. Modelling of the undisturbed boundary layer (trade cumulus and stratocumulus) has also progressed with improved understanding of cloud-scale transports and the coupled radiative fluxes.

The wide diurnal variation of the radiative cooling rate in the tropical atmosphere has caused considerable speculation on the role of radiative forcing and the coupling of radiative and convective transports.

The analysis and synthesis of results from GATE will take many years and fill many volumes. This review will cover only a few topics which the author understands a little better now than five years ago. The main themes will be one day in GATE (2 September 1974); squall-line and downdraught structure; and the budget approach to analysis.

* Address now: West Pawlet, Vermont 05775.

2. Discussion of one day in GATE: 2 September 1974

This day, on which organized precipitating convection developed in the B scale array, illustrates several features of convection in GATE, some of which are not well understood. This day has been discussed in Mower (1977) and Mower *et al.* (1978) from which some of the figures are taken or adapted. The general features discussed are common to much of the convection in GATE, even the stronger squall-line cases, which have been explored in Houze (1977), Zipser (1977), Zipser and Gautier (1978), GATE Workshop (1977). Figure 1 shows the positions of the GATE B and A/B scale ships during phase III.

Figures 2(a) and (b) show an overview from the SMS satellite at 12 and 17 z. Figures 3(a) and (b) show mosaics at 13 and 16 z constructed from the four C band radars showing the bands of precipitation themselves.

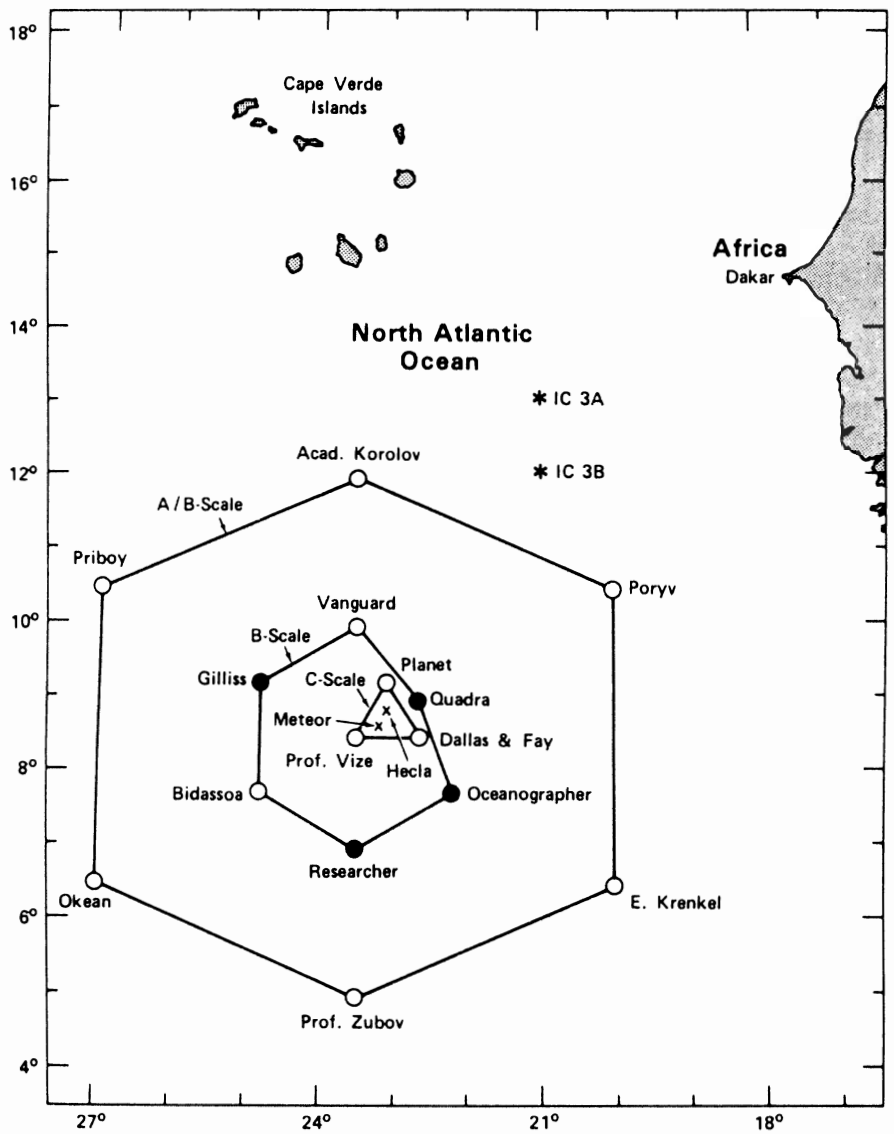

Figure 1. B and A/B scale ship positions during phase III of GATE. Solid circles mark ships with C band radars used in the radar composites and rainfall estimates.

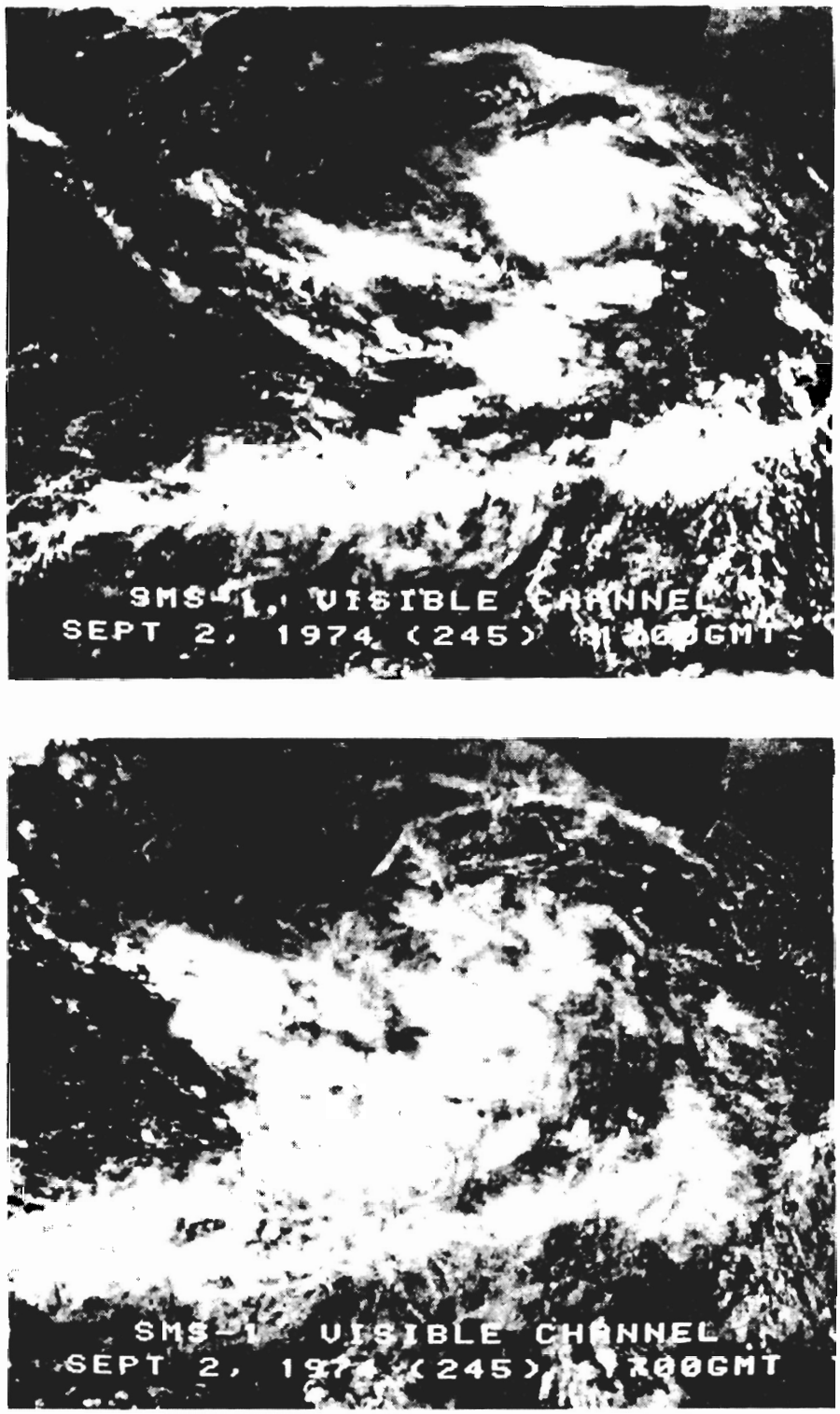

Figure 2. Visible images from SMS–1 satellite at 12 and 17z on 2 September 1974.

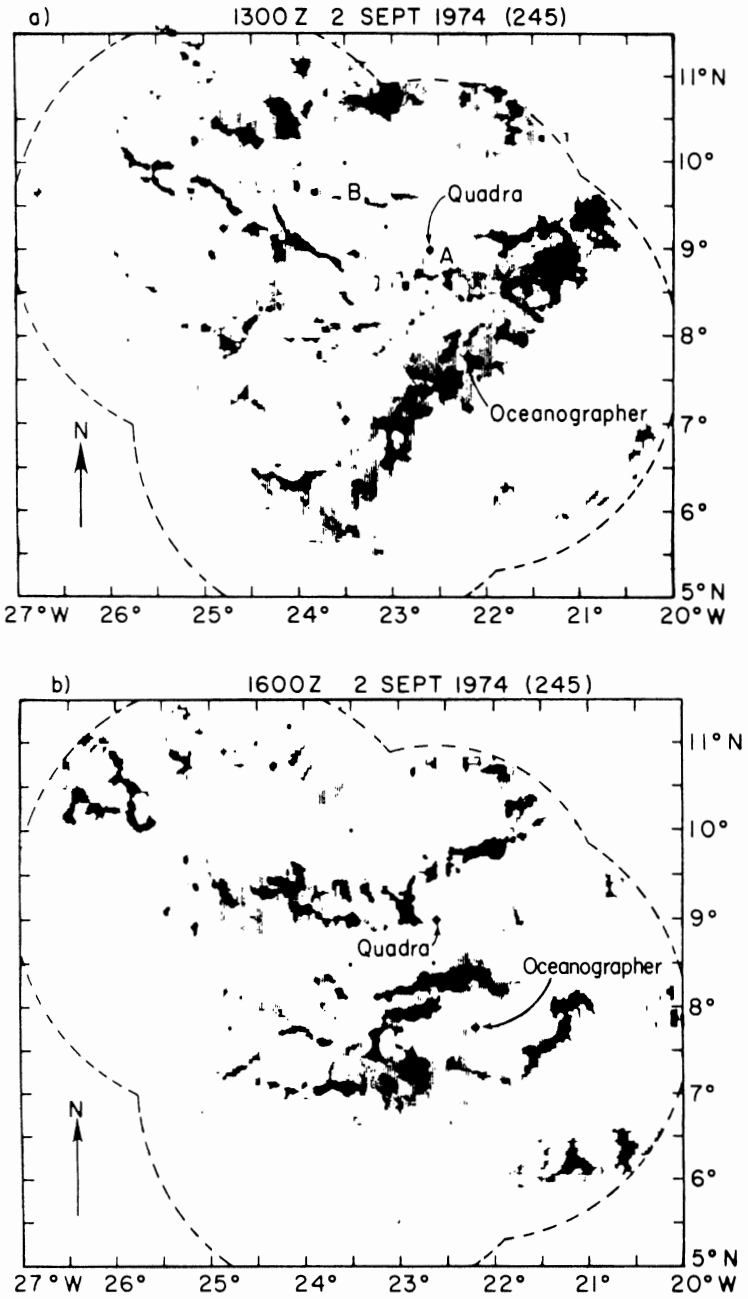

Figure 3. Radar mosaics at 13 and 16 z constructed from the four C band radars (Fig. 1). (Produced by F. Marks.)

(a) Viewed from the synoptic scale, there is rapid growth of bands of convection just ahead of the trough axis of the 700 mb large-scale wave. The convective bands grow rapidly from about 06 to 18 z, when the typical cirrus shield of a cloud cluster obscures the banded structure on a satellite picture (see Fig. 2(b) at 17 z), and then convection decays rapidly in the period 18 to 24 z. The broad band oriented SW to NE in Fig. 3(a) is

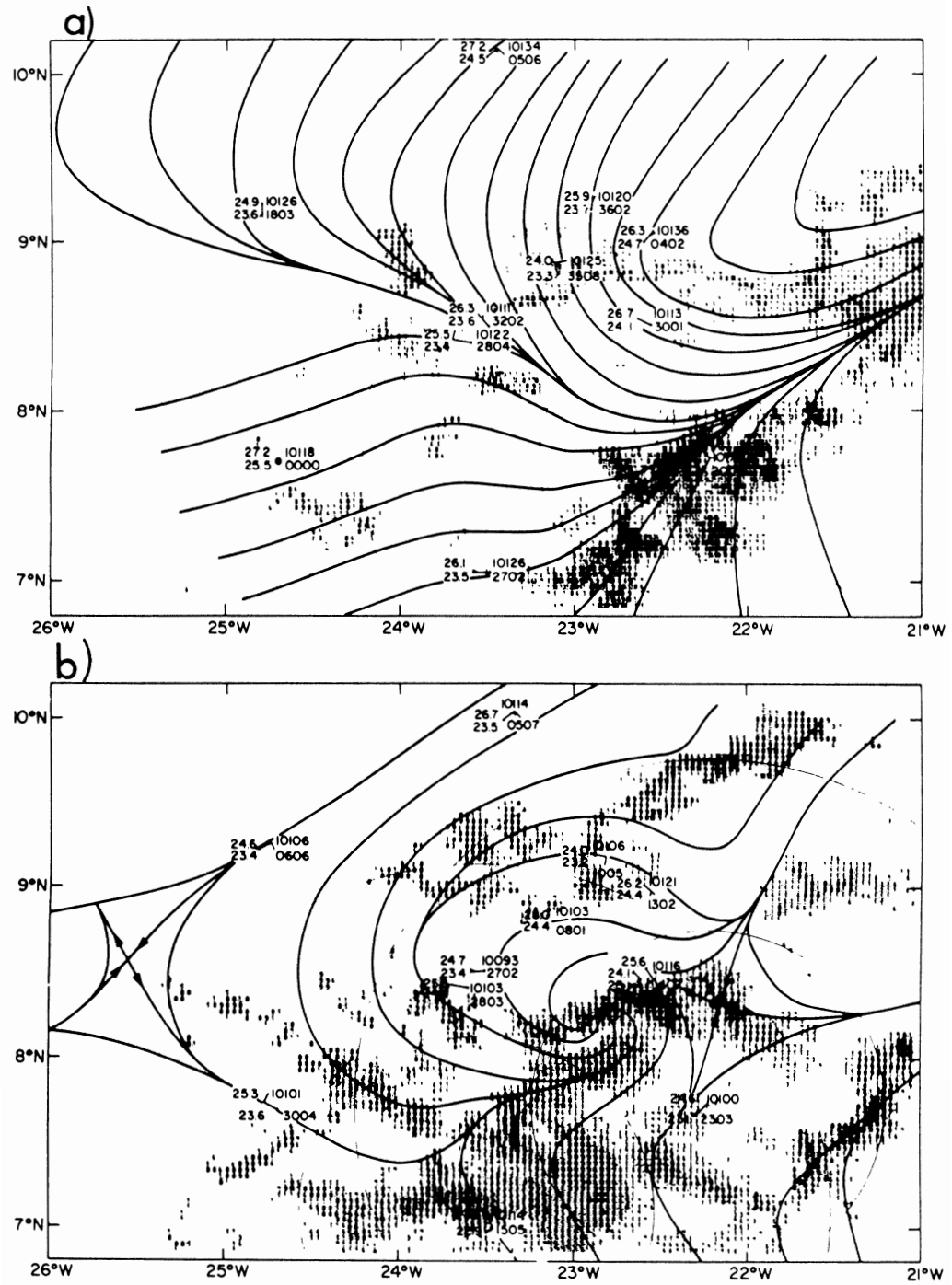

Figure 4. Surface streamline analysis for (a) 12z and (b) 16z from WMO data set overlaid on hybrid radar data from *Oceanographer* and *Researcher* (from Mower *et al.* 1978).

aligned roughly along the surface trough and is moving westwards. This could be regarded as the main band of the ITCZ.

(b) On the meso-synoptic-scale, a surface meso-cyclone appears between 14 and 15 z. Figures 4(a) and (b) show surface streamline analyses at 12 and 16 z overlaid on a radar picture. This suggests a dynamic feedback from the convective scale, producing cyclogenesis.

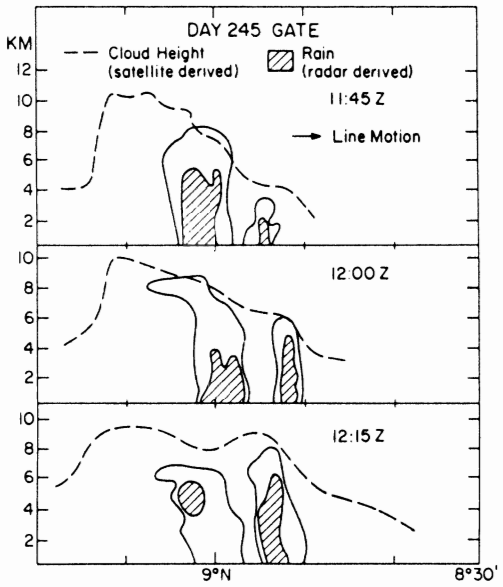

Figure 5. Cross-sections through the convective line along the aircraft flight tracks (north–south on 22°51'W) on 2 September 1974, showing sequential growth of new cells on the leading edge (from Mower *et al.* 1978).

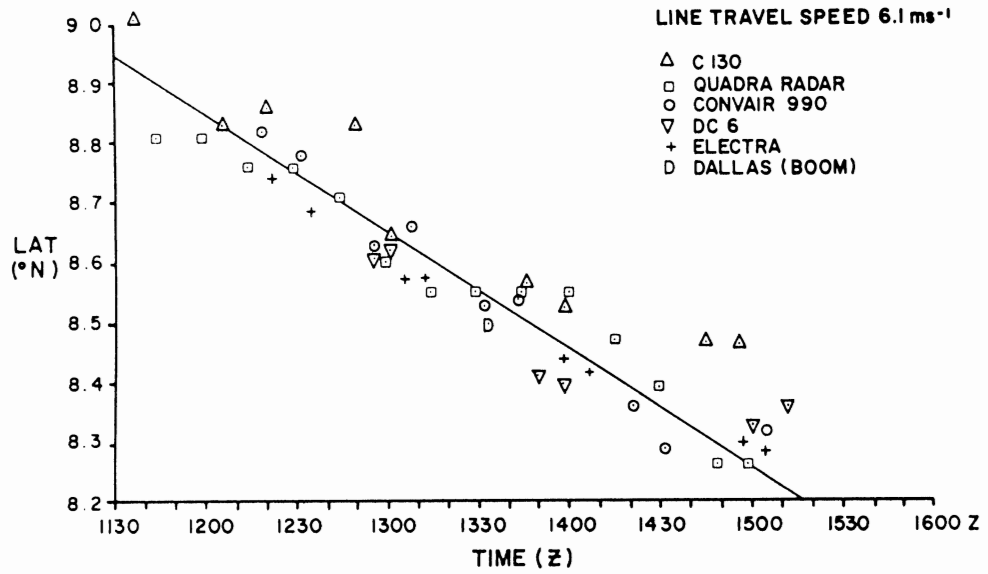

Figure 6. Mean travel speed of convective line A derived from least-squares fit of data marking line passage as a function of latitude and time. The boom on ship *Dallas*, and the low-level aircraft (Electra and DC-6), indicate position of low-level wind shift or gust front; the *Quadra* radar, the leading edge of the precipitation; and the other aircraft, C-130 and Convair 990, the convective towers behind the surface gust front (from Mower 1977).

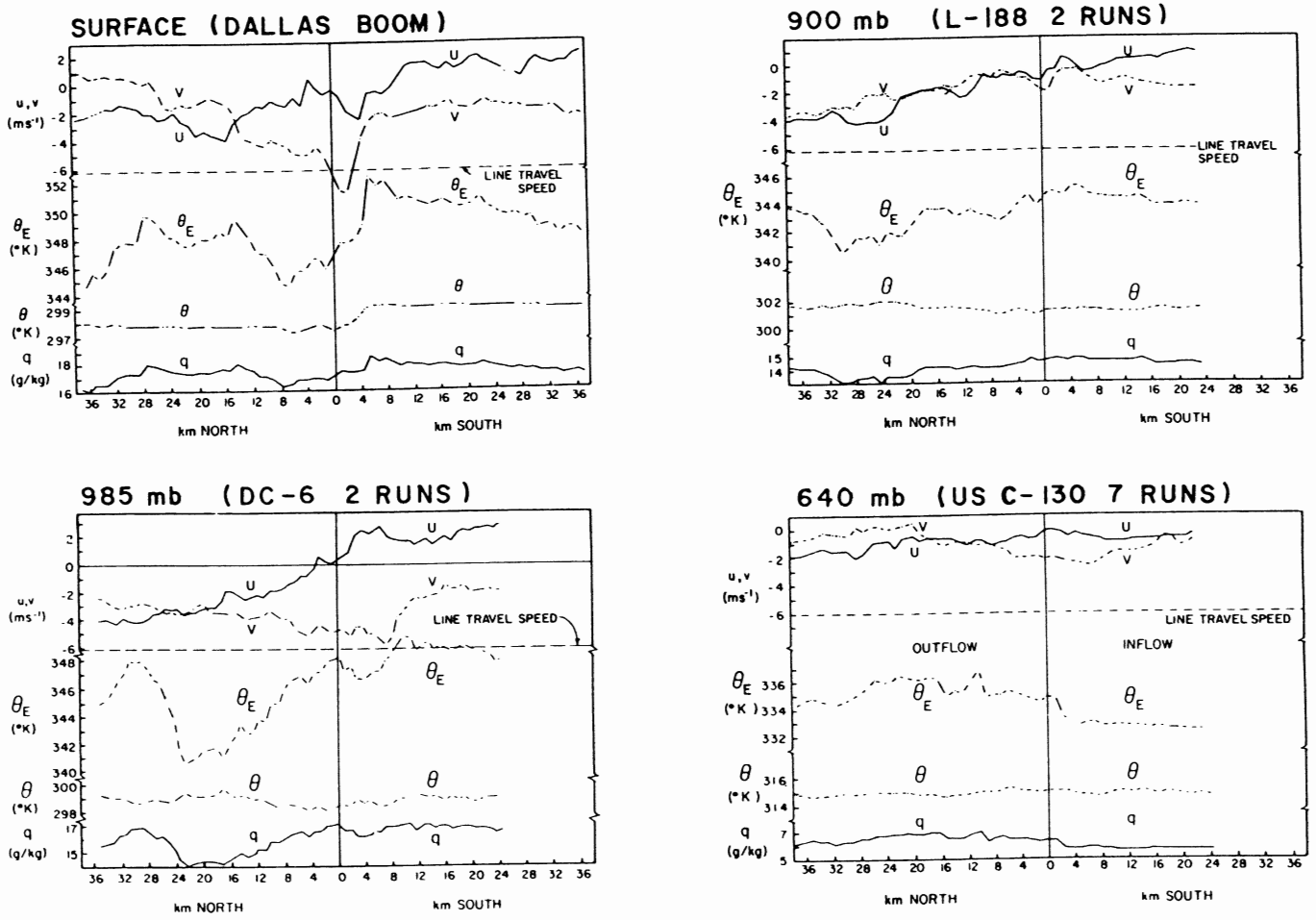

Figure 7. Time and space series relative to convective line A at different pressure levels. Surface cross-section is a time series at the boom of the ship *Dallas* converted to a space series using line speed of $6\,m\,s^{-1}$ southward (Fig. 6). Above the surface are shown average space cross-sections from north–south aircraft runs, composited with respect to the mean latitude–time position of the convective line (Fig. 6) (from Mower 1977).

However, after the formation of the meso-cyclone the convection soon reaches its peak and decays, suggesting that the dynamic development is unable to organize further intensification. This seems to have been the case in almost all cases of meso-cyclone development in GATE, and clearly needs further study.

(c) Viewed from the mesoscale, one sees travelling convective bands (although some move slowly). These bands move with the speed of their surface gust front, and move by the successive growth of new cells on the leading edge (Fig. 5). The cells themselves do not share the propagation speed of the line. On Fig. 3(a) two lines are marked, A and B, which are both propagating southwards at about $6\,m\,s^{-1}$ (Fig. 6 shows this motion for line A). The mechanism of propagation is not clear. In some respects it resembles the gust front propagation of a surface density current as in squall-lines (see section 3(*a*)), but the observed temperature fall at the low-level wind shift (observed both by aircraft and ship systems (Fig. 7)) is rather small (2 K at the surface). Also, both lines can be traced back towards the cloud echo to the north (Fig. 3). In particular, line B is identifiable as a cloud arc at 12 z travelling at about $6\,m\,s^{-1}$, *before* it is visible on the radars. This suggests that a propagating wave is organizing the convection but is largely independent of it. The bands feed from the front and the strongest precipitation is at the leading edge. Figure 7 shows 2-D cross-sections across line A. It is associated with 2-D cyclonic vorticity ($\sim 10^{-4}s^{-1}$) and low-level convergence (as high as $10^{-3}s^{-1}$ near the gust front), with a broader divergent area to the rear (the north) under downdraughts from decaying cells and anvil precipitation. At low levels there is a characteristic fall of θ_E associated with the passage of the system and the replacement of subcloud layer air of high θ_E with cooler, drier downdraught air, of lower θ_E. At mid-levels (640 mb) there is a rise of θ_E behind (northward of) the line gust-front (which is at approximately the 0 km line).

(d) On the cloud- and sub-cloud-scale, aircraft occasionally penetrate strong cloud-scale updraughts and downdraughts (up to $4\,m\,s^{-1}$). The analysis of heat, moisture and momentum fluxes associated with these is still in progress. (For an example of a strong updraught, see Zipser and Gautier 1978.)

We are still a considerable way from an adequate description of, let alone a satisfactory theoretical model for, the nonlinear interactions between these various scales of instabilities. The next section will discuss some conceptual models which have proved useful in interpreting the observed phenomena.

3. Models and concepts

(*a*) *Squall-line structure*

The tropical squall-line has received considerable study over the past few years, and a good conceptual appreciation of its mesoscale structure has emerged (Betts 1976a; Betts *et al.* 1976; Moncrieff and Miller 1976; Miller and Betts 1977; Zipser 1969, 1977; Houze 1977; Mansfield 1977). In most respects this structure is the same as that of the travelling lines discussed in section 2, only the convection is more intense.

Figure 8 (adapted from Houze 1977) shows a schematic structure. Squall-lines have relative inflow from the front as they propagate through the air. They move by the discrete growth of new line elements ahead of old ones (Houze 1977). The growth of new cells is organized along the spreading gust front, itself fed by downdraughts from decaying cells (Moncrieff and Miller 1976). The high-level outflow streams off to the rear, and precipitation from the anvil forms a large region of nearly stratiform rain behind the leading edge. There is some evidence of mesoscale ascent in the middle–upper troposphere, helping maintain the anvil, and good evidence of lower troposphere mesoscale descent under the anvil. It is not clear whether this mesoscale downdraught is primarily dynamically driven (Miller

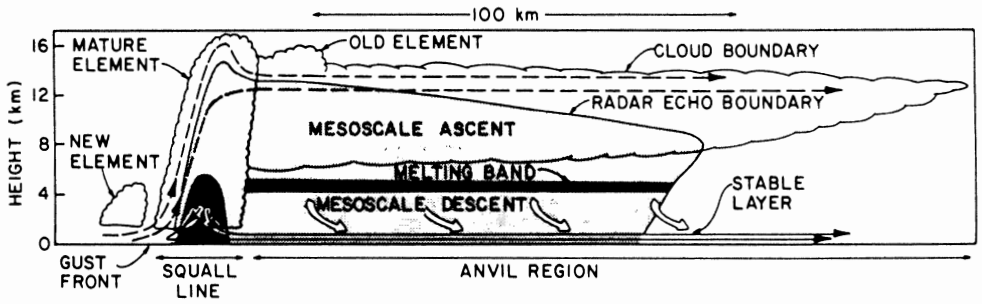

Figure 8. Schematic cross-section through squall-line system. Streamlines show flow relative to the squall-line. Dashed streamlines show updraught circulation, thin solid streamlines show convective-scale downdraught circulation associated with mature squall-line element, and wide arrows show mesoscale downdraught below the base of the anvil cloud. Dark shading shows strong radar echo in the melting band and in the heavy precipitation zone of the mature squall-line element. Light shading shows weaker radar echoes. Scalloped line indicates visible cloud boundaries (from Houze 1977).

and Betts 1977) or driven by the evaporation of falling precipitation (Riehl 1969; Zipser 1969, 1977). This mesoscale downdraught, which often is warm and dry by the time it reaches 900–950 mb, is undercut by cooler relatively moister downdraught air which probably descended in cloud-scale downdraughts in the squall-line (Fig. 8). Zipser (1977) shows a more detailed schematic structure. The low-level mixed layer of high θ_E is swept up into the cloud and probably ascends with a little dilution to the upper troposphere. It is replaced by lower θ_E air, with a more complex structure resulting from cloud- and meso-scale downdraughts: a cool, moist layer underlying a warmer, much drier layer. The inversion between the two layers caps the lower layer, which becomes well mixed over the warm ocean and grows into the sinking dry stable layer above by entrainment processes. The mixing down of drier air from the layer above means that the minimum 10 m dewpoint is reached sometime after the passage of the squall front. It takes many hours for the re-establishment of an oceanic mixed layer capped by small cumulus, as shown by accoustic sounder records (Gaynor and Mandics 1978).

Using data over land (VIMHEX) and smoothing the detailed outflow structure by using layer averages, Betts (1976a) showed how the boundary layer transformation warm–moist → cool–dry could be interpreted quantitatively from a mean trajectory conserving θ_E as the sum of two processes: a descent trajectory from above cloud base, and the evaporation of falling precipitation. The first process introduces warmer drier air into the low levels, while the second cools and moistens it. Typically the average effect which results from the ambient stratification preceding the squall-line and the amount of evaporation is that the new boundary layer air is drier (i.e. descent dominates) but also cooler (i.e. evaporative cooling dominates) than the warm, moist squall inflow (see Fig. 9).

The origin of the inflow into the downdraughts is unclear in two respects (which are not shown in Fig. 8): the level and the direction of relative inflow to the squall-line. Typically squall-lines move into the ambient air at the front at all levels (Betts *et al.* 1976; Zipser 1977), which suggests that downdraught air flows into the storm from the front and wraps around and under the updraught, as is modelled in Moncrieff and Miller (1976). Betts (1976a) suggested that the downdraught inflow layer is the 100–150 mb layer above the inflow subcloud layer. Zipser (1977) suggested that the cloud-scale downdraught may come from this layer being swept into the storm with some mixing between updraught and downdraught with subsequent descent driven by evaporation of precipitation, particularly of small cloud droplets (to maintain near saturation). However, the same papers (and Houze 1977) also show middle tropospheric inflow into the rear of the squall-line feeding

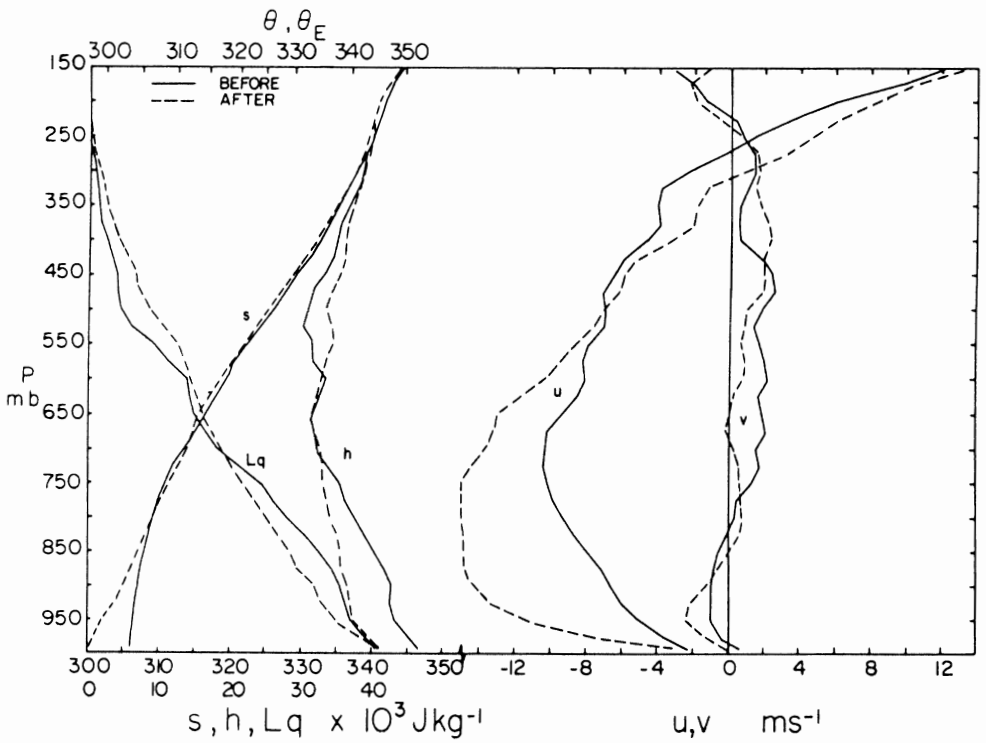

Figure 9. Mean tropospheric profiles of static energy s, moist static energy h, water vapour (as latent energy Lq), and wind components u, v, before and after the passage of a travelling convective storm over the rawinsonde site. The upper scale shows potential temperatures θ, θ_E, corresponding with slight approximation to s and h (from Miller and Betts 1977).

perhaps mesoscale ascent and mesoscale descent circulation under the anvil. Thus, the two downdraught circulations may involve inflow into the squall-line from both the front and the rear. Inflow from the front may involve air flowing around updraught cores, with discrete propagation through the development of new line elements, so that air may find itself behind the new squall leading edge; or a time sequence may be involved with the main entrainment into downdraughts occurring as cells collapse and decay. Mid-level inflow from the rear has been simulated as a mesoscale feature (Brown 1978). It seems likely that as in mid-latitudes these two dimensional models are not sufficient to describe the three dimensional structure of the squall-line.

The dynamic aspects of tropical squall-lines are less well understood than are the thermodynamic aspects. Over Venezuela they form in a sheared environment, typically with a wind maximum in the lower middle troposphere parallel to and comparable with the motion vector of the squall-line. Figure 9 shows composite u, v wind profiles and thermodynamic profiles before and after the passage of travelling (squall-type) systems over Venezuela (Miller and Betts 1977). The low-level acceleration of the u flow behind the squall throughout a deep layer to a speed close to (and sometimes greater than) that of the squall is apparent (the average squall system travel speed was $13\,m\,s^{-1}$). There is a reverse acceleration at upper levels. This is an up-gradient momentum transport modelled and discussed in Moncrieff and Miller (1976). We do not yet understand the relationship of this mesoscale momentum transport to the synoptic scale momentum (and vorticity) budgets.

One further fundamental question posed before GATE, which we cannot yet answer,

is whether for the parameterization of convection in synoptic models we need to allow for the mesoscale organization of the convection into bands and lines, or whether the integral over an entire band or squall-line is not distinguishable on the synoptic scale from an ensemble of independent convective cells.

(*b*) *Modelling downdraught thermodynamics*

In the thermodynamic budget, convective downdraughts are important because of their downward mass transport, their re-evaporation of some of the precipitation condensed in the updraught, and their dramatic transformation of the boundary layer which may in turn increase the surface fluxes. A simple parametric downdraught model needs to specify three factors: level of origin of downdraught, downdraught mass flux, and the thermodynamic profiles in the downdraught. The first is clearly difficult and may require a source function as a function of height. The second is fundamentally related to the three-dimensional structure and dynamics of a squall-line and the overall precipitation efficiency, but we do not have a general understanding. Betts (1976a) and Johnson (1976) have suggested using the ratio (downdraught mass flux) to (updraught mass flux) as a measure of bulk precipitation efficiency. A model for the third factor (the thermodynamic profiles in the downdraught) has been proposed by Betts and Silva Dias (1978). They show that the thermodynamic paths, $q(p)$ and $\theta(p)$, of an unsaturated downdraught (suffix 'd') can be computed using a pressure scale (Π_E) related to rainfall rate, drop size spectrum and downdraught speed:

$$(\partial q/\partial p)_d = \Delta q/\Pi_E, \quad (\partial\theta/\partial p)_d = \Delta\theta/\Pi_E, \tag{1}$$

where $\Delta q = q_w(T_w) - q_d$, $\Delta\theta = \theta_w(T_w) - \theta_d$, and q_w, θ_w are the saturation mixing ratio and potential temperature at the downdraught wet bulb temperature (assumed to be the temperature of the evaporating drops) which lies on the downdraught path of constant

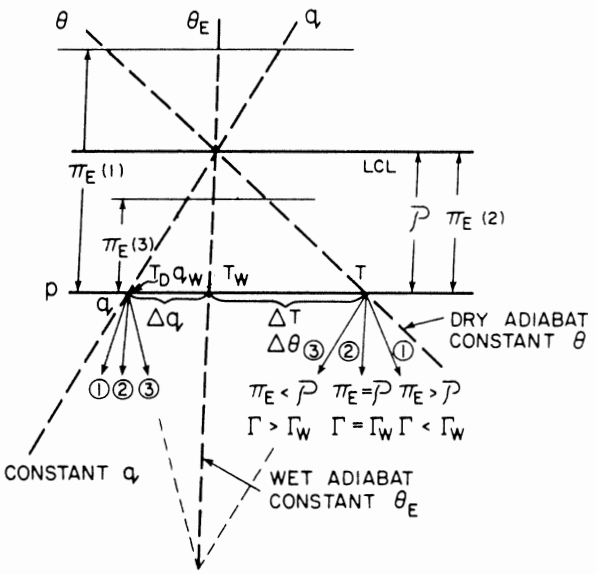

Figure 10. Schematic tephigram showing initial downdraught descent paths (thin solid lines) for different magnitudes of evaporation scale Π_E ($> \bar{P}$, $= \bar{P}$, $< \bar{P}$), labelled (1), (2) and (3) respectively. Paths (3) for small Π_E intersect at saturation on wet adiabat if projected (light dashed lines), as do lines (1) if projected back (not shown). Light dotted lines are construction lines parallel to descent paths (1) with slopes $\Delta q/\Pi_E(1)$, $\Delta\theta/\Pi_E(1)$. $\Pi_E(3)$ is shown, but construction lines for paths (3) are omitted (from Betts and Silva Dias 1978).

equivalent potential temperature. The pressure scale Π_E can be regarded as a bulk downdraught parameter. It can (in principle) be computed from rainfall rate, drop size spectrum and downdraught speed (Betts and Silva Dias 1978), but in modelling may have to be specified based on diagnostic studies. Given Π_E these equations can be integrated to give the downdraught path of $q(p)$, $\theta(p)$, if downdraught inflow properties are known, since q_w, θ_w then lie on a known θ_E adiabat. Equation (1) can be summarized on a tephigram (Fig. 10). It is helpful to note that the pressure difference $\mathscr{P}$ to the lifting condensation level (LCL) can be expressed using a pair of equations similar to (1):

$$(\overline{\partial q_w/\partial p})_{\theta_E} = \Delta q/\mathscr{P} \text{ and } (\overline{\partial \theta_w/\partial p})_{\theta_E} = \Delta\theta/\mathscr{P}, \quad . \quad . \quad (2)$$

where on the left we linearize the gradients of saturation mixing ratio and potential temperature on the wet adiabat. It is clear from (1) and (2) that the relationship of $\mathscr{P}$ to Π_E determines that of the downdraught trajectory to the wet adiabat. If $\Pi_E > \mathscr{P}$, $(\partial\theta/\partial p)_d < (\partial\theta_w/\partial p)_{\theta_E}$; $(\partial q/\partial p)_d < (\partial q_w/\partial p)_{\theta_E}$ and the downdraught paths will be those marked (1) in Fig. 10. We note the temperature path is between the wet and dry adiabats and the air becomes more unsaturated. These paths can be constructed from knowledge of Π_E as parallels to the dotted lines which denote the gradients $\Delta q/\Pi_E$ and $\Delta\theta/\Pi_E$. If $\Pi_E = \mathscr{P}$ then the downdraught paths for q and θ both parallel the wet adiabat (marked (2)): the downdraught path is one of constant relative humidity and $\mathscr{P}$. This is the asymptotic state if Π_E is constant.

If $\Pi_E < \mathscr{P}$, then paths marked (3) result: the temperature path is more stable than the wet adiabat and the downdraught approaches saturation on the θ_E adiabat. These solutions are discussed in more detail in the paper cited.

The modelling problem can thus be closed by specifying inflow properties and Π_E, but we are still dependent on diagnostic studies to determine these. Typical values of Π_E range from about 20 mb for near-saturated cloud-scale downdraughts to 100 mb for strongly unsaturated downdraughts.

(*c*) *Budget studies*

A key GATE objective was the computation of bulk convective sources and sinks of water and energy from rawinsonde data using the budget method (Reed and Recker 1971; Nitta 1972; Holland and Rasmusson 1973; Yanai *et al.* 1973). Studies have been published using the wave composite method (Reed *et al.* 1977; Norquist *et al.* 1977) and the A/B scale ship data (Nitta 1977). The poor quality of the Navaid ship winds may limit the quality of budgets based on B scale ship data alone. The calculation of apparent sources and sinks of heat and moisture as budget residuals from $T(p)$, $q(p)$, $\mathbf{V}(p)$ fields as resolved by the rawinsondes is straightforward, although different ways of smoothing the sounding data in time and space are possible. The interpretation of these derived bulk convective sources using cloud models has been the subject of much research. Yanai *et al.* (1973) used a cloud mass flux model to interpret the convective sources. Ogura and Cho (1973) and Nitta (1975) used the spectral cloud model proposed by Arakawa and Schubert (1974) to derive a cloud mass flux distribution function for a spectrum of cloud sizes. Betts (1975) discussed the conserved thermodynamic variables and suggested that the apparent sources should be integrated to a flux form where (in the absence of cloud-scale storage of heat and water) the constraints on the convective fluxes at the surface and the top of the convective layer (where they should vanish) are more clearly visible. In this flux form the convective heating rate is still visible as the gradient. The importance of cloud storage terms in a developing field of convection (on the mesoscale) was discussed by McNab and Betts (1978). Johnson (1976) and Nitta (1977) introduced downdraughts into the spectral cloud

model, and with differing assumptions derived a downdraught mass flux as well as that of updraughts. As was shown in the previous two sections, downdraughts play an important role in the modification of the boundary layer. One composite budget study (Betts 1973a) estimated that the downdraught mass flux was about half that of the updraught in mesoscale cumulonimbus systems over Venezuela.

It is difficult to say what these studies have taught us about precipitating tropical convection. The convective sources derived from budgets are almost, so to speak, an observable: the models used for their interpretation are highly idealized and interpret these sources in terms of model parameters, which may not be readily observable. For example, it is difficult to envisage how model-derived cloud population spectra can be compared satisfactorily with the observed time-dependent cloud distributions organized into mesoscale bands in the budget volume. Attempts are being made to reverse the process and derive comparison budgets by integration (using a cloud model) from cloud fields observed by radar (Houze and Leary 1976).

Furthermore, it is not yet clear what degree of detail in the convective model is sufficient for parameterization in a prognostic model. The cloud mass flux concept represented a significant advance in modelling. It has greatly improved our understanding of shallow convection (see section 3(*d*)). For shallow non-precipitating convection, the budget studies have shown that the convective fluxes of total water and energy can be modelled quite well using the convective mass flux concept. For precipitating convection, we do not understand well enough what controls the vertical distribution of the precipitation flux (that is, the distribution of condensation, transport and evaporation of liquid water averaged over the life-cycle of a cloud, and a mesoscale system). Since this precipitation flux dominates the water transport and enthalpy transport (that is liquid water static energy or potential temperature transport) we have been able to do little to interpret these transports unambiguously. The moist static energy flux is independent of the liquid water flux, but its structure depends critically on *two* variables – updraught and downdraught mass fluxes, so these cannot be diagnosed uniquely. It appears that the definitive interpretation of budget studies for precipitating convection requires further insight or at least an improved parametric model for the interrelation of the bulk precipitation flux and the convective mass fluxes (updraught and downdraught).

GATE A/B scale budgets for 2 September 1974 will illustrate these remarks. As discussed in section 2, organized mesoscale convection developed in the A/B scale ship array, reached a peak, and subsequently decayed. Figure 11 shows the integrated precipitation rate over the GATE master array (Richards and Hudlow 1977) – a 200 km radius circle centred on 8°30′N 22°30′W – derived from the four C band radars. The rapid growth in precipitation from 10 to 18 z as the convection intensified (and the mesoscale vortex formed) is apparent. The heavy dots shown for comparison are satellite precipitation estimates for the A/B scale array derived from SMS satellite data (Stout and Martin 1977), calibrated in part against the radars. The radar master array is somewhat smaller than the A/B scale ship hexagon, but the rain rates are probably representative as indicated by the satellite estimates, since the cluster development was well centred in the array. Also in Fig. 11 is the integrated A/B scale apparent convective heat source (converted to $\mathrm{mm\,h^{-1}}$) from rawinsonde budgets computed by Nitta (1978), and radiation budgets by Cox and Griffith (1978) (see also Fig. 14). The heat source integrated over the day is equivalent to precipitation of 24·6 mm (or 685 $\mathrm{W\,m^{-2}}$ in Fig. 13), very close to the integrated precipitation estimate by radar of 24·2 mm. The surface sensible heat flux is negligible (equivalent to $\sim$0·5 mm of precipitation) in comparison, so this heat source can be identified as a net condensation.

Although it is perhaps stretching the rawinsonde data too far to interpret the time sequence of budgets (they were also subjected to a low-pass filter), the time sequence is

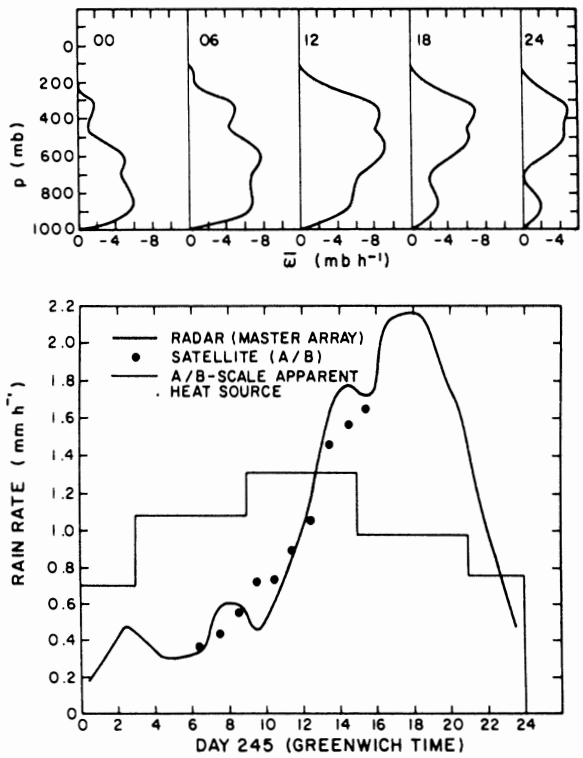

Figure 11. Comparison between radar rain rates (heavy curve) for the 'master array', satellite-derived rain rates for the A/B scale ship array (dots), and integrated A/B scale apparent heat source (block). Upper curves are A/B scale average vertical motion profiles at 6 h intervals for 2 September 1974.

suggestive. The net condensation heat source peaks about six hours ahead of the precipitation maximum, suggesting that an increased storage of liquid water in the atmosphere in clouds is an important contribution to the convective budget. This stored water is subsequently precipitated as the cloud cluster decays. This inferred liquid water storage in clouds (6·2 mm in 15 hours, equivalent to a 275 W m^{-2} energy flux) is equivalent to about a 34% increase in cloud cover in 15 hours of clouds with integrated liquid water content of 2 g cm^{-2}. This seems a little high. However, the change in cloud cover was very rapid. Figure 12 shows the percentage of visible cloud tops below specified pressure levels derived from SMS infrared data in conjunction with radiation budget estimates (Cox and Griffith 1978). The percentage cover of deep clouds in the A/B scale array (tops to 400 mb) increased by 65% from 0430 to 1630 z, although these areas are biassed by cirrus cover and overestimate cloud volume integrated through the troposphere.

Figure 11 also shows the time sequence of mean vertical motion profiles (Nitta 1978). At 00 z on 2 September there is strong upward motion in the lower troposphere (in fact a large increase from 18 z on the 1st). This upward motion strengthens and deepens to a peak at 12 z when the rainfall rate is increasing in the lower troposphere. By 06 z on the 3rd (not shown) there is weak descent at 700 mb and the ascent in the upper troposphere has fallen below 2 mb h^{-1}. This pattern fits the growth and decay of the deep convection very well, and it seems that though $\bar{\omega}$ may initially force the growth of organized mesoscale convection, the subsequent profiles are more the convective response: that is, the integrated convective mass transport. In particular, the decay of upward motion in the lower troposphere

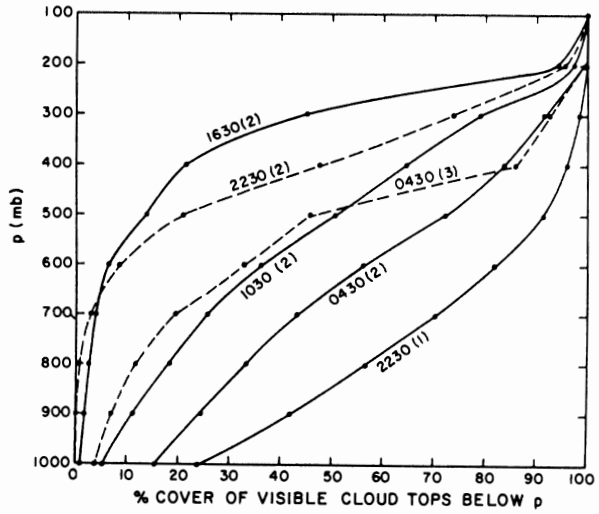

Figure 12. Percentage cover of cloud tops below a pressure level from 2230 z on 1 September to 0430 z on 3 September at 6 h intervals, derived from SMS–1 infrared data. The ordinate at 1000 mb is the percentage clear sky. The last two curves are shown dashed for clarity.

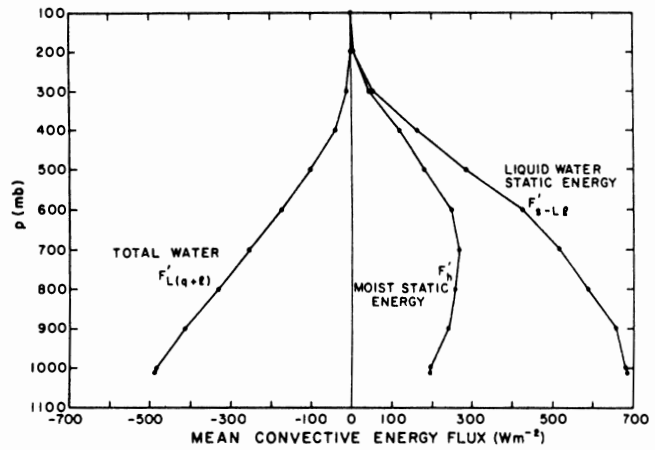

Figure 13. 24-hour-average profile of convective energy fluxes for 2 September 1974 (integrated apparent source terms), derived from A/B scale budgets.

later in the day presumably reflects the development of convective and mesoscale downdraughts, discussed in section 3(*a*). More cases need to be studied before firm conclusions can be drawn.

Figures 13 and 14 show the integrated convective source terms: the integrals of cloud storage and vertical convective flux divergence, which have been given the symbols

$$F'_h = \int (Q_1 - Q_2 - Q_R)(dp/g) \quad . \quad . \quad . \quad (3a)$$

$$F'_{L(q+l)} = \int -Q_2(dp/g) \quad . \quad . \quad . \quad . \quad (3b)$$

$$F'_{s-Ll} = \int (Q_1 - Q_R)(dp/g) \quad . \quad . \quad . \quad (3c)$$

The integrals are from 100 mb to P; suffixes denote the conserved thermodynamic variables: moist static energy h, total water (vapour q plus liquid l) times latent heat L, static energy s minus Ll; and Q_1, Q_2, Q_R are the conventional symbols for apparent heat source, vapour sink and the radiational heating rate. In the absence of storage of heat and water in the cloud fields, these integrals represent the A/B average convective fluxes (Betts 1975) and have surface values equal to the surface fluxes of moist static energy, latent heat flux minus precipitation (in energy units) and sensible heat flux plus precipitation. Figure 13 shows the 24-hour averaged profile in which cloud storage processes are probably small. These curves indicate, as expected, that the cloud cluster is a heat source and a vapour sink through precipitation, and transports a greater moist static energy flux upwards through 700 mb than the surface sensible plus latent heat flux. This removal of h from the low levels is accomplished by the high-h updraught and low-h downdraught circulations. The heating profile is, however, dominated by the precipitation flux, while in the water transport both the vapour and liquid fluxes are important. Figure 14 shows the progression of F_h' etc. during the day, but the surface values of F_h' are rather low in the early morning and rather high at 18 z. These are exactly the differences to be expected from increasing storage of h in clouds during the initial cluster growth and decreasing storage as the cloud systems decay. The average value of F_h' for the day is 196 W m^{-2} (Fig. 13), similar (perhaps a little high) to other disturbed days in GATE (GATE workshop, 1977). Taking 196 W m^{-2} as a representative surface flux of h, one may estimate the storage term as equivalent to 150 W m^{-2} for the nine hours 00 to 09 z. For comparison with the estimate of liquid water storage, this corresponds to a 22% increase in nine hours in cloud cover of clouds 500 mb deep with mean excess water vapour of 2 g kg^{-1} (an integrated excess vapour content of 1 g cm^{-2}). These numbers seem reasonably consistent, although it should be repeated that firm conclusions cannot be drawn from one day's rawinsonde data. A detailed interpretation would require a cloud model for this storage, for the precipitation flux and for the updraught and downdraught mass fluxes, as well as study of other cases.

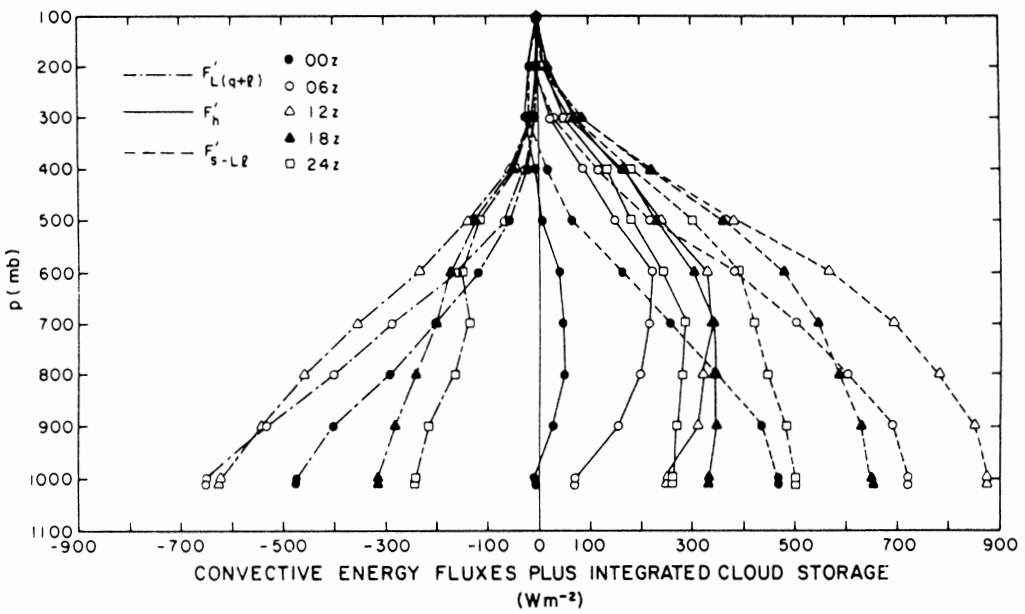

Figure 14. Integrated apparent convective sources/sinks of water, moist static energy and heat (see Eqs. (3)) for 6 hourly sequence of A/B scale budgets for 2 September 1974. These integrals represent convective energy fluxes plus integrated cloud storage.

Clearly the interpretation of these time-dependent budgets needs great care. Moreover the time change of the synoptic fields is a residual of the convective fluxes and storage, the radiative fluxes (themselves coupled to the convection), and the large-scale advection, which are all nearly but not quite in balance – although it is precisely this imbalance that determines the subsequent dynamic development of the synoptic scale. It is not yet clear whether the detailed understanding of cloud-scale transports, which we endeavour to extract from diagnostic studies, is essential for prognostic parameterization, or whether some of this detail can be avoided by the use of simple closures or a quasi-equilibrium assumption (as in Arakawa and Schubert 1974). This is near the heart of the scale interaction objective of GATE, and it needs further descriptive theoretical analysis.

(*d*) *Trade cumulus*

Our understanding of trade cumulus convection has advanced considerably in recent years. The importance of cumulus transports in maintaining the trade inversion against the large-scale subsidence in the descending branch of the Hadley circulation (Riehl and Malkus 1957) has been confirmed. The cumulus clouds cool and moisten the warm, dry air as it descends across the inversion. Non-precipitating cumulus clouds transport water upwards and heat downwards (through condensation, upward advection and evaporation of liquid water (Betts 1973b)). This is a destabilizing process, which tends to deepen the cloud layer, but in the trades it is balanced by the drying, stabilizing effect of the large-scale subsidence. Viewing the layer below cloud top as a whole, the cumulus clouds *transport* heat, but are almost a zero net *source* of heat (condensed liquid water is nearly all re-evaporated, with little precipitation). The small surface heat flux and the adiabatic warming by the mean subsidence are balanced by radiative cooling from the moist subcloud and cumulus layers.

These balances are the basis of computations of cumulus fluxes by the budget method. Mean profiles and fluxes in the tradewind layer are given in Fig. 15, based on Holland and Rasmusson (1973), Nitta and Esbensen (1974), Betts (1975). The (negative) gradients of the convective flux profiles give the warming and moistening by the convection. The cloud layer has two distinct regions: a lower more unstable layer (see $\bar{h}_s$ profile, h_s being saturated static energy) which is warmed and slightly moistened by the convection, and an upper stable layer (often an inversion) which is cooled and strongly moistened by the cumulus.

The interpretation of these fluxes has been the subject of many papers (Nitta 1975; Betts 1973b, 1975; Soong and Ogura 1976). Figure 15 also shows a convective mass flux above cloud base. This is the mean mass flux in the clouds which, multiplied by cloud–environment differences of total water, liquid water static energy and moist static energy (derived from an entraining cloud model), gives (to good approximation) the convective fluxes in Fig. 15 (Betts 1975). Thus, for non-precipitating clouds it seems that a single upward mass transport coupled with a cloud model is sufficient to specify the convective transports. Nitta (1975) gave a spectral decomposition of this mass flux in terms of clouds which have different entrainment rates (following the model of Arakawa and Schubert 1974). This study, and Fig. 15, show that the detrainment of 'cloudy air' is important throughout the cumulus layer, even though there are peaks in the trade inversion layer and near cloud base. Betts (1975) showed that the representation of a flux, for example of liquid water static energy, s_l,

$$gF'_{s-Ll} = gF'_{s_l} = -\overline{\omega' s'_l} = \omega^*(s_{lc} - \bar{s}), \qquad (4)$$

as the product of a cloud mass flux parameter ω^* and a cloud–environment difference

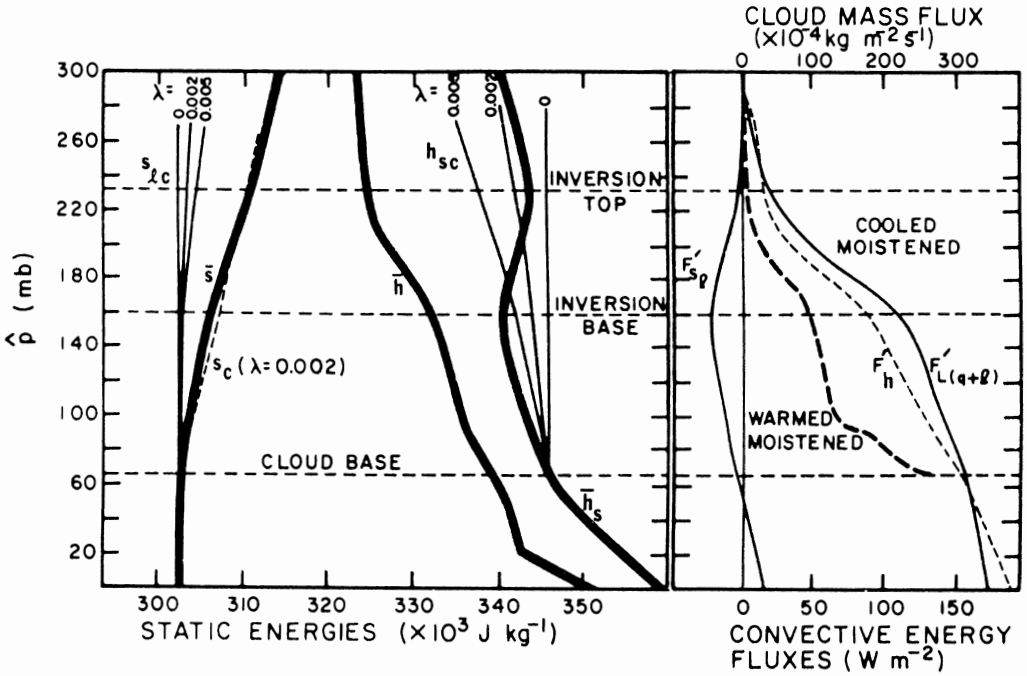

Figure 15. Mean static energy profiles for 5-day BOMEX tradewind average environment (heavy lines), in-cloud parcel paths (light lines) for different fractional entrainment rates (λ) are shown on left. On the right are convective energy fluxes and mass flux above cloud base (heavy dashed line), for $\lambda = 0{\cdot}005$.

$(s_{lc}-\bar{s})$, where subscript 'c' relates to a single entraining cloud parcel, implies that the convective heating rate can be split into two terms:

$$Q_1 - Q_R = g\,\partial F'_{s_l}/\partial p = -\omega^*\,\partial\bar{s}/\partial p + \mu\omega^*(s_{lc}-\bar{s}), \quad . \quad . \quad (5)$$

where μ is a scale length for detrainment (in pressure units). The first can be regarded as the compensating subsidence of the environment (which warms) and the second the detrainment of cloud static energy and liquid water to the environment as the cloud mass flux decreases. This is a cooling term since the water evaporates. Since the gradient of F'_{s_l} changes sign in Fig. 15 near the base of the trade inversion, we infer that the first term dominates in the lower cloud layer, and as ω^* decreases and $(s_{lc}-\bar{s})$ increases, the second dominates in the upper cloud layer.

A parcel path model is helpful in providing a different 'explanation' of this same process of warming below and cooling above (Betts 1973b), and in giving some insight into the mechanism by which a cloud modifies the environment during its lifecycle. Figure 16 is a schematic tephigram showing parcel paths, and environmental profiles of θ_E, θ_L, $q+l$. These are nearly conserved in isobaric mixing, and in adiabatic (dry or moist) ascent or descent (θ_L, $q+l$ are conserved only if no fallout of liquid water occurs). Figure 16 shows the ascent and descent paths for a model cloud parcel with properties T_L, θ_L, T_W, θ_E, T_{DT}, $q+l$ (see appendix) calculated using a constant entrainment rate of 100% in 100 mb from the BOMEX 5-day-mean profile (Holland and Rasmusson 1973). The effect of mixing below cloud base is small because the subcloud layer is itself nearly well-mixed. The three parcel paths intersect at the LCL or cloud base (where liquid water first becomes non-zero), and then diverge. If there were no entrainment, the three paths would follow the dry adiabat, wet adiabat and constant q path as in Fig. 19 (appendix). With entrainment the θ_L path is found by mixing cloud θ_L (which was θ at cloud base) with environment $\bar{\theta}$ (assuming it

has no liquid water); the θ_E path (θ_{ES} while saturated) by mixing cloud $\theta_{E(S)}$ with the environment $\bar{\theta}_E$; and the cloud total water by mixing with the drier environment $\bar{q}$: for each path the same mixing or entrainment rate is used.

Figure 16 shows parcel ascent and overshoot of its zero buoyancy level and subsequent descent, with entrainment continuing. The cloud paths come together again after descent at what we might call the SEL (sinking evaporation level) where liquid water is again zero. The paths cross: θ_L becomes θ again; θ_{ES}, θ_E and $q_s + l$ just q. A second level of near-neutral buoyancy is reached (p_N) and further damped oscillations of the now unsaturated parcel can be expected. Figure 16 shows that for a realistic entrainment rate a parcel following this path is close to neutrally buoyant on descent to the inversion base and has almost reached the mixing ratio of the environment. In this and some other cases the parcel is still moister than the environment: a slightly larger entrainment rate would remove this difference, but make it warmer than the environment. It is possible that radiative cooling of cloud parcels descending from cloud top plays a role in the approach to equilibrium (as in section 3(*e*) on stratocumulus).

We can, thus, envisage a steady buoyantly driven circulation in which the model cloud takes air from below cloud base, mixes it with cloud layer air and detrains at the inversion base with near environmental properties. The modification of the environment is then effected only by its vertical circulation. There is a double cell environmental circulation: sinking below the final cloud-air equilibrium level producing warming and drying,

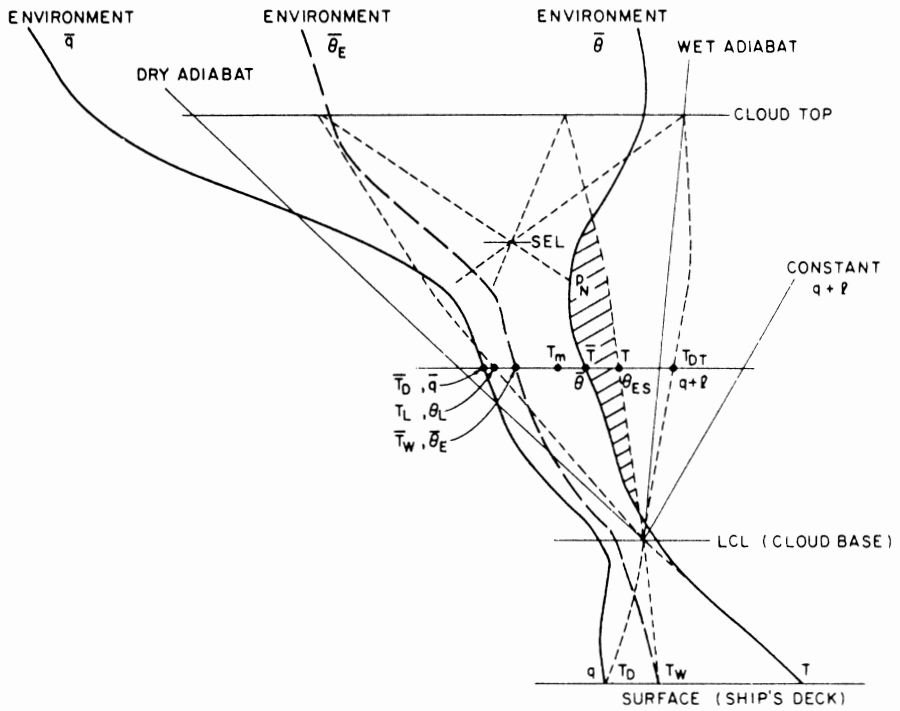

Figure 16. Five-day-mean BOMEX average environment profiles of T, θ_E, and q (heavy lines) plotted on a tephigram. The light dashed lines are schematic convective parcel paths (cumulus above cloud base). These show ascent with entrainment from the surface through cloud base (at their lifting condensation level after mixing) up to cloud top followed by descent with continued mixing through the sinking evaporation level (SEL) where the paths intersect and the visible coud disappears. These parcel paths are arbitrarily terminated when the descending parcel again reaches thermal equilibrium with the environment. At one level a temperature T_m is shown: it is the lowest temperature obtainable by mixing cloud and environment in such a ratio that all the cloud liquid water just evaporates.

and rising motion above producing cooling and moistening (in the upper layer the cloud parcel brings down more air than it takes up because of entrainment). This model 'explains' the pattern of warming and cooling in Fig. 15 but cannot explain why the entire cloud layer is moistened. In the moisture budget equation corresponding to Eq. (5),

$$-Q_2 = g\,\partial F'_{L(q+l)}/\partial p = -L\omega^*\,\partial\bar{q}/\partial p + \mu\omega^* L(q_c + l_c - \bar{q}), \qquad (6)$$

the second term on the right is larger than the first even in the lower cloud layer where μ is small: that is, detrainment cannot even be qualitatively neglected in the water budget. There is a significant water vapour input into the lower cloud layer, either from smaller clouds which do not reach the trade inversion, or from the fact that all clouds are rather transient. Only some of the moist air rising through cloud base follows the path in Fig. 16, as the cloud soon dies, leaving a column of vapour and liquid to be mixed into the environment. In the average over the lifecycle this is a contribution to the detrainment, μ (see Fraedrich 1973, 1976; Betts 1975; Cho 1977).

Figure 16 can be used to study cloud–environment mixing processes at one level. For example, mixing at cloud boundaries produces cooling through evaporation. The lowest temperature that can be reached occurs when after mixing one unit of cloud with ε units of the environment, all the cloud water *just* evaporates leaving a just saturated mixture cooler and moister than the environment. This is denoted by a *single* point on the tephigram, denoted, T_m (since at saturation $T = T_D = T_W = T_L$). This temperature and ε can easily be found on the diagram, since

$$\frac{T_L - T_m}{T_m - \bar{T}} = \frac{q + l - q_s(T_m)}{q_s(T_m) - \bar{q}} = \frac{\theta_{ES} - \theta_{ES}(T_m)}{\theta_{ES}(T_m) - \bar{\theta}_E} = \varepsilon. \qquad (7)$$

This tephigram representation (which also shows the positive available potential energy per unit mass as the shaded area) plus the mass flux concept of cumulus transports are invaluable tools in the study of convective transports by shallow convection in the tropics.

(*e*) *Stratocumulus*

A similar diagrammatic approach will summarize our understanding of a well-mixed layer of stratocumulus. Here again the cloud circulation is the transport mechanism for heat and moisture between the sea surface and the subsidence inversion at cloud top. There are three main differences from a layer of scattered cumulus:

(i) The solid cloud cover concentrates the radiative cooling (and shortwave absorption during the day) to a shallow layer near cloud top.

(ii) The cloud layer now contains roughly equal ascending and descending branches both filled with cloud. This layer is nearly well mixed in the vertical in the conserved thermodynamic parameters (θ_E, $q+l$, θ_L), and mixing between ascending and descending branches can probably be neglected in modelling.

(iii) The dominant entrainment process of mixing of cloudy air with warm dry air is now confined to the inversion top where mixing and radiative cooling occur together.

Lilly (1968) and Schubert (1976) have discussed the modelling of a layer of stratocumulus. Schubert *et al.* (1977) have shown schematic parcel paths for air in a steady-state stratocumulus layer, driven by radiative cooling (and evaporative mixing) above, over a cooler ocean. These diagrams can be summarized on one tephigram (Fig. 17). For a unit parcel, θ_E, θ_L and total water are conserved on the ascent path from the surface to the top of the stratocumulus layer. However, at the top of the layer, mixing and radiative cooling occur: both non-conservative processes which change the parcel properties (reducing total water, θ_E, and increasing θ_L in the case shown) before the descent path which is again

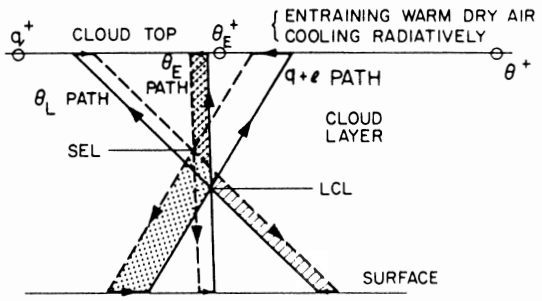

Figure 17. Schematic ascent paths (solid) and descent paths (dashed) for air parcels in a well-mixed stratocumulus layer over a cooler ocean. Mixing and radiative cooling occur at the cloud top inversion, overlain with warm dry air (properties shown by open circles). The radiative cooling forces convective descent through the cloud layer to the sea surface where the now warm dry air picks up moisture and loses some heat to the cool ocean. The SEL on descent is above the LCL on ascent, because of the diabatic process and mixing at cloud top. The shaded areas are related to the water vapour flux (dotted) and sensible heat flux (line shading).

conservative. The path cycle is completed at the surface where the parcel picks up moisture from the ocean but is cooled (in the case shown, the ocean is cooler than the air).

In the steady state, the convective fluxes are constant between the surface and the inversion: they are the mechanism which transfers energy from the surface to moisten and cool the warm, dry air subsiding through the strong inversion at cloud-top. The 'mean profiles' in the stratocumulus layer could be constructed as the average of ascending and descending branches (if equal areas of up and down motion are assumed). In this steady-state 'mixed' model the conserved fluxes, the intensity of the mass circulation (ω^*) and the corresponding conserved up–down parcel differences are all *constant* between surface and cloud top. The areas between up and down circulations are related to the magnitude of the fluxes, i.e.

$$F_{q+l} = (\omega^*/g)[(q+l)_u - (q+l)_d] \quad . \quad . \quad (8)$$

$$F_{\theta_E} = (\omega^*/g)(\theta_{Eu} - \theta_{Ed}) \quad . \quad . \quad . \quad (9)$$

$$F_{\theta_L} = (\omega^*/g)(\theta_{Lu} - \theta_{Ld}) \quad . \quad . \quad . \quad (10)$$

where suffices 'u' and 'd' denote up and down parcel properties. The diagram also shows the area related to the water vapour flux (dot shading) and the sensible heat flux (line shading), while the liquid water flux can also be seen as the difference of two triangular areas (between total water and water vapour paths, or θ and θ_L paths).

Figure 17 also shows that on descent the SEL is reached before the LCL on ascent: that is, the entrainment of dry air at the cloud top, and change of temperature, mean that in the descending branch of the stratocumulus circulation all the liquid water evaporates (and cloud disappears) above the cloud base for the ascending branch. One might ask: what determines the difference between the up and down curves and hence the pressure difference between LCL and SEL? Clearly, it is the entrainment at cloud top, which is itself related in the steady state to the mean sinking at that level. One may write for the water balance at cloud top, assuming equal areas of up and down motion,

$$\omega^*(q_{Tu} - q_{Td}) = -\bar{\omega}[\tfrac{1}{2}(q_{Tu} + q_{Td}) - q^+], \quad . \quad . \quad (11)$$

where $q_T = q + l$ and q^+ is the water vapour above the inversion at cloud top. This equation says the flux carried by the cloud circulation must supply water to the mean sinking of dry air through the inversion. The difference

$$(q_{Tu}-q_{Td}) = -(\bar{\omega}/\omega^*)\delta q \quad . \quad . \quad . \quad (12)$$

where $\delta q = \frac{1}{2}(q_{Tu}+q_{Td})-q^+$, depends on the ratio of $\bar{\omega}$ to the cloud circulation. The more intense the circulation, the smaller the difference between the up and down branches; while conversely, if the circulation is slow, $q_{Tu}-q_{Td}$ becomes large and in some limit the cloud might all evaporate near cloud top, breaking up the stratocumulus layer. The intensity of the cloud circulation could be determined from the available potential energy (itself related to the virtual temperature flux).

The transport mechanism from surface to subsidence inversion, summarized in Fig. 17 for a stratocumulus layer, has many similarities to that in the cumulus layer. It represents a limit in which ascending and descending areas are comparable, cloud filled and well mixed, so that the convective circulation parameter ω^*, rather than being a strongly decreasing function of height as it is for scattered cumulus (Fig. 15), can be modelled as constant. The stratocumulus layer is also similar to a well-mixed dry convective layer (see next subsection).

(*f*) *Convection in the subcloud layer*

Mixed layer models (similar to Lilly (1968) for stratocumulus) have been used extensively to describe the growth of an inversion-capped layer of dry convection (Betts 1973b; Carson 1973; Tennekes 1973; Esbensen 1975; and others). These involve a mixed layer budget with a closure condition that the downward virtual heat flux at the top of the mixed layer is minus some fraction $\beta \sim 0{\cdot}2$ times the surface virtual heat flux. Comparisons with numerical simulations (Deardorff 1974) show good agreement in predicting boundary layer height, and mean temperature rise.

Betts (1976b) has suggested from a VIMHEX budget study that a convective mass flux can be defined in the subcloud layer (Fig. 18). It rises from zero in the surface superadiabatic layer, is roughly constant through the mixed layer and then falls rapidly below cloud base in the transition layer between the well-mixed highly turbulent layer and the stratified cumulus layer penetrated by widely spaced clouds. The crosses with bars in Fig. 18, derived from GATE aircraft data (Nicholls and LeMone 1978), fit the dimensionless mass flux profile from the VIMHEX budget rather well – there is a factor of about ten difference in the surface heat flux between the tropical land and oceanic cases.

Cumulus clouds are well rooted in the mixed layer (Betts *et al.* 1974; Johnson 1976; LeMone and Pennell 1976) but Fig. 18 shows that much of the subcloud layer turbulence is trapped in the subcloud layer. For very shallow clouds and clouds over a heated land surface the stabilization at cloud base is the control mechanism (Betts 1973b). It is maintained by convective heating above cloud base, which is related to a convective mass flux out of the subcloud layer. If this mass flux into the cloud layer becomes too large, then the stabilization increases, and reduces the cloud base mass flux. This control diminishes for deep convection which has a large potential energy source in the cloud layer. Over ocean, the surface virtual heat flux is very small, and correspondingly virtual temperature fluctuations and the cloud base stabilization are also small. In this situation even for shallow cumulus (and of course, for stratocumulus over a cold ocean) the clouds may be primarily driven by buoyancy in the cumulus layer.

4. Final remarks

A lot more is known about convection in the tropics as a result of field experiments of the past decade. Broad similarities in cumulus convection at all latitudes are becoming

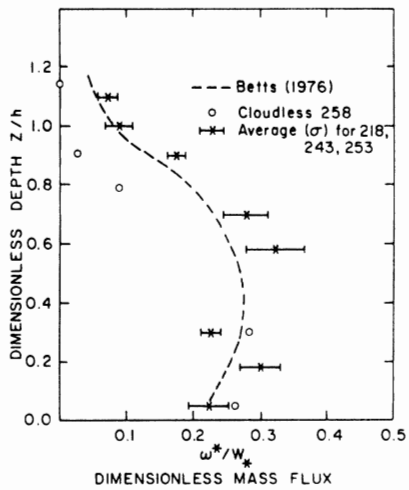

Figure 18. Dimensionless convective mass flux profile in subcloud layer plotted against dimensionless depth. Scaling parameter W_* is convective velocity scale (mass flux units) and h is depth of subcloud layer (turbulent layer for cloudless day). The heavy dashed line is from Betts (1976b), the open circles for a cloudless day in GATE (Julian Day 258), and the crosses are three-day averages (with standard deviations) for days 218, 243, 253 in GATE (from Nicholls and LeMone 1978).

apparent, and conceptual models are being developed for the range of convective scales from shallow dry convection to thunderstorm scale. This review has addressed only a small part of the whole. It seems, however, that the simpler problems of a dry convective boundary layer, shallow cumulus and stratocumulus controlled by the surface, larger-scale vertical motion and radiation, are now understood more thoroughly than the more complex problem of precipitating convection organized on the mesoscale. The study of this was, of course, a key GATE objective. A descriptive basis for study now exists but new ideas come slowly. The nonlinear interactions between meso- and cloud-scales and between meso- and synoptic-scales need further study, as does the relation of the cloud-scale precipitation to other cloud-scale transports. Momentum and vorticity transport by clouds has hardly been addressed in this paper. A definitive model still seems elusive, although there has been some progress in the last few years.

The basic GATE modelling question, as to how well the smaller-scale convective processes can be parameterized in numerical models, cannot yet be answered.

Acknowledgments

One cannot acknowledge by name all those who contributed to the tropical field experiments of the past decade. Some of the research discussed in this review was supported by the National Science Foundation and the GATE Project Office of NOAA, under grant ATM 77–15369. The writing and presentation of this review has been supported by this same grant, and in part by a Sloan Fellowship.

References

Amirov, A. D. 1971 Calculation of humidity and temperature fields in the problem of a cumulus, *Izvestiya, Atmospheric and Oceanic Physics*, 7, 723–730.

Arakawa, A. and Schubert, W. 1974 Interaction of a cumulus cloud ensemble with the large-scale environment. Part I, *J. Atmos. Sci.*, 31, 674–701.

Betts, A. K.	1973a	Non-precipitating cumulus convection and its parameterization, *Quart. J. R. Met. Soc.*, **99**, 178–196.
	1973b	A composite mesoscale cumulonimbus budget, *J. Atmos. Sci.*, **30**, 597–610.
	1974	The scientific basis and objectives of the U.S. convection subprogramme for the GATE, *Bull. Amer. Met. Soc.*, **55**, 304–313.
	1975	Parametric interpretation of trade-wind cumulus budget studies, *J. Atmos. Sci.*, **32**, 1934–1945.
	1976a	The thermodynamic transformation of the tropical subcloud layer by precipitation and downdrafts, *Ibid.*, **33**, 1008–1020.
	1976b	Modelling subcloud layer structure and interaction with a shallow cumulus layer, *Ibid.*, **33**, 2363–2382.
Betts, A. K., Dugan, F. J. and Grover, R. W.	1974	Residual errors of the VIZ radiosonde hygristor as deduced from observations of the subcloud layer structure, *Bull. Amer. Met. Soc.*, **55**, 1123–1125.
Betts, A. K., Grover, R. W. and Moncrieff, M. W.	1976	Structure and motion of tropical squall-lines over Venezuela, *Quart. J. R. Met. Soc.*, **102**, 395–404.
Betts, A. K. and Silva Dias, M. F.	1978	Unsaturated downdraft thermodynamics in cumulonimbus, submitted to *J. Atmos. Sci.*
Brown, J. M.	1978	Mesoscale unsaturated downdrafts driven by rainfall evaporation: A numerical study, accepted for publication in *J. Atmos. Sci.*
Carson, D. J.	1973	The development of a dry inversion-capped convectively unstable boundary layer, *Quart. J. R. Met. Soc.*, **99**, 450–467.
Cho, Han-Ru	1977	Contributions of cumulus cloud life-cycle effects to the large-scale heat and moisture budget equations, *J. Atmos. Sci.*, **34**, 87–97.
Cox, S. K. and Griffith, K. T.	1978	Tropospheric radiative divergence during Phase III of the GARP Atlantic Tropical Experiment (GATE), Colorado State University *Atmospheric Science Paper 291.*
Deardorff, J. W.	1974	Three-dimensional numerical study of the height and mean structure of a heated planetary boundary layer, *Bound. Layer Met.*, 7, 81–106.
Esbensen, S.	1975	An analysis of sub-cloud-layer heat and moisture budgets in the Western Atlantic trades, *J. Atmos. Sci.*, **32**, 1921–1933.
Fraedrich, K.	1973	On the parameterization of cumulus convection by lateral mixing and compensating subsidence. Part I, *Ibid.*, **30**, 408–413.
	1976	A mass budget of an ensemble of transient cumulus clouds determined from direct cloud observations, *Ibid.*, **33**, 262–268.
GATE Central Program Workshop Report	1977	Held at the National Center for Atmospheric Research, Boulder, Colorado, 25 July–12 August 1977, under the sponsorship of the National Science Foundation and National Oceanic and Atmospheric Administration.
Gaynor, J. E. and Mandics, P. A.	1978	Analysis of the tropical marine boundary layer during GATE using acoustic sounder data, *Mon. Weath. Rev.*, **106**, 223–232.
Haman, K.	1973	On the notion of equivalent specific liquid water content and its applications to the thermodynamics of clouds, *J. Appl. Met.*, **12**, 1129–1133.
Holland, J. Z. and Rasmusson, E. M.	1973	Measurements of the atmospheric mass, energy and momentum budgets over a 500-kilometer square of tropical ocean, *Mon. Weath. Rev.*, **101**, 44–55.
Houze, R. A. Jr. and Leary, C. A.	1976	Comparison of convective mass and heat transports in tropical easterly waves computed by 2 methods, *J. Atmos. Sci.*, **33**, 424–429.
	1977	Structure and dynamics of a tropical squall-line system, *Mon. Weath. Rev.*, **105**, 1540–1567.
Johnson, R. H.	1976	The role of convective-scale precipitation downdrafts in cumulus and synoptic scale interaction, *J. Atmos. Sci.*, **33**, 1890–1910.

LeMone, M. A. and Pennell, W. T. 1976 The relationship of trade-wind cumulus distribution to sub-cloud layer fluxes and structure, *Mon. Weath. Rev.*, **104**, 524–539.

Lilly, D. K. 1968 Models of cloud-topped mixed layers under a strong inversion, *Quart. J. R. Met. Soc.*, **94**, 292–309.

McNab, A. and Betts, A. K. 1978 A mesoscale budget study of cumulus convection. Accepted for publication in *Mon. Weath. Rev.*

Mansfield, D. A. 1977 Squall-lines observed during GATE, *Quart. J. R. Met. Soc.*, **103**, 569–574.

Miller, M. J. and Betts, A. K. 1977 Travelling convective storms over Venezuela, *Mon. Weath. Rev.*, **105**, 833–848.

Moncrieff, M. W. and Miller, M. J. 1976 The dynamics and simulation of tropical cumulonimbus and squall-lines, *Quart. J. R. Met. Soc.*, **102**, 373–394.

Mower, R. N. 1977 Case study of convection lines during GATE. Colorado State University *Atmospheric Science Paper 271*. NTIS Document PB–272 943.

Mower, R. N. *et al.* 1978 A case study of GATE convective activity. Submitted to *Atmosphere*.

Nicholls, S. and LeMone, M. A. 1978 The fair weather boundary layer in GATE. (Manuscript in preparation, title tentative.) To be submitted to *J. Atmos. Sci.*

Nitta, T. 1972 Energy budgets of wave disturbances over the Marshall Islands during the years 1956 and 1958, *J. Met. Soc. Japan*, **50**, 71–84.

1975 Observational determination of cloud mass flux distributions, *J. Atmos. Sci.*, **32**, 73–91.

1977 Response of cumulus updraft and downdraft to GATE A/B-scale motion systems, *Ibid.*, **34**, 1163–1186.

1978 Personal communication.

Nitta, T. and Esbensen, S. 1974 Heat and moisture budgets using BOMEX data, *Mon. Weath. Rev.*, **102**, 17–28.

Norquist, D. C., Reed, R. J. and Recker, E. E. 1977 The energetics of African wave disturbances as observed during Phase III of GATE, *Ibid.*, **105**, 334–342.

Ogura, Y. and Cho, H. R. 1973 Diagnostic determination of cumulus cloud populations from observed large-scale variables, *J. Atmos. Sci.*, **30**, 1276–1286.

Reed, R. J. 1978 The structure and behaviour of easterly waves over West Africa and the Atlantic (this volume).

Reed, R. J. and Recker, E. E. 1971 Structure and properties of synoptic-scale wave disturbances in the equatorial Western Pacific, *J. Atmos. Sci.*, **29**, 1117–1133.

Reed, R. J., Norquist, D. C. and Recker, E. E. 1977 The structure and properties of African wave disturbances during Phase III of GATE, *Mon. Weath. Rev.*, **105**, 317–333.

Richards, I. and Hudlow, M. 1977 Use and abuse of the GATE digital radar set. Preprint volume of the *11th Tech. Conf. on Hurricanes and Tropical Meteorology*, December 1977, Miami, Florida.

Riehl, H. 1969 Some aspects of cumulonimbus convection in relation to tropical weather disturbances, *Bull. Am. Met. Soc.*, **50**, 587–595.

Riehl, H. and Malkus, J. S. 1957 On the heat balance and maintenance of the circulation in the trades, *Quart. J. R. Met. Soc.*, **83**, 21–29.

Sarachick, E. S. 1974 The tropical mixed layer and cumulus parameterization, *J. Atmos. Sci.*, **31**, 2225–2230.

Schubert, W. H. 1976 Experiments with Lilly's cloud-topped mixed layer model, *Ibid.*, **33**, 436–446.

Schubert, W. H., Wakefield, J. S., Steiner, E. J. and Cox, S. K. 1977 Marine stratocumulus convection, Colorado State University *Atmospheric Science Paper 273*. NTIS Document PB–272 955.

Soong, S-T. and Ogura, Y. 1976 A determination of the tradewind cumuli population using BOMEX data and an axisymmetric cloud model, *J. Atmos. Sci.*, **33**, 992–1007.

Stout, J. and Martin, D. 1977 Rainfall estimation from geostationary satellite images over the GATE area. Preprint volume of *11th Tech. Conf. on Hurricanes and Tropical Meteorology*, December 1977, Miami, Florida.

Tennekes, H. 1973 A model for the dynamics of the inversion above a convective boundary layer, *J. Atmos. Sci.*, **30**, 558–567

Yanai, M., Esbensen, S. and Chu, J. 1973 Determination of bulk properties of tropical cloud clusters from large-scale heat and moisture budgets, *Ibid.*, **30**, 611–627.

Zipser, E. T. 1969 The role of organized unsaturated convective downdrafts in the structure and rapid decay of an equatorial disturbance, *J. Appl. Met.*, **8**, 799–814.

1977 Mesoscale and convective scale downdrafts as distinct components of squall-line structure, *Mon. Weath. Rev.*, **105**, 1568–1589.

Zipser, E. T. and Gautier, C. 1978 Mesoscale events within a GATE tropical depression, *Ibid.*, **106**, 789–805.

APPENDIX

CUMULUS THERMODYNAMICS ON THE TEPHIGRAM

(*a*) *Introduction*

The tephigram, along with other thermodynamic diagrams, has long been a useful operational and theoretical aid to the understanding of atmospheric stability, cumulus structure and transports. However, incomplete use is usually made of the tephigram once air becomes saturated. The purpose of this appendix is to discuss some conventions and parameters which permit an extension in its use. These extensions are primarily of advantage in handling non-precipitating cumulus and stratocumulus.

One must distinguish between parameters from which the tephigram is *constructed*: temperature, T, pressure, p, and those derived from T and p – potential temperature $\theta(p,T)$, saturation mixing ratio, $q_s(T,p)$, saturation equivalent potential temperature, $\theta_{ES}(T,p)$; and those parameters which we plot on the tephigram by convention. The distinction is a fine one. One point (T,p) on the diagram represents air temperature, pressure, θ, q_s, θ_{ES}. When we plot dewpoint on the temperature axis, this is a convention – valuable because the mixing ratio $q = q_s(T_D)$ is represented. Similarly the plot of wet bulb temperature (T_W,p) also plots θ_E on the θ_{ES} coordinates, because $\theta_E(T,p,q) = \theta_{ES}(T_W,p,q_w)$. Other conventions are possible: for example, one could plot equivalent temperature θ_E using the (T,θ,p) coordinates as a point far to the right of the air temperature.

(*b*) *Liquid water potential temperature and an extended dewpoint definition*

Betts (1973b) introduced the liquid water potential temperature, θ_L, defined in a way similar but opposite to θ_E, as the potential temperature that could be reached by evaporating all the liquid water in a parcel, together with the convention of plotting it on (θ,p) coordinates. If a parcel is moved vertically adiabatically, and there is no fallout of liquid water, some of these plotted parameters are conserved (θ_L if saturated; θ if unsaturated; θ_{ES} if saturated; θ_E if unsaturated; q_s+l if saturated, where l is liquid water; q if unsaturated); but not others (T, T_D, T_W for example). Figure 19 shows these parameters as they change in adiabatic ascent across a saturation level (e.g. cloud base). It is clear that for continuity we should continue to plot *dewpoint* T_{DT} above cloud base representing *total* water (q_s+l). This is an acceptable convention: it is still the temperature at which the air is just saturated (although to form dew, we must heat past this temperature and then cool slightly!). We have also defined a liquid water temperature T_L corresponding to (θ_L,p). Amirov (1971) defined a similar function of convenience in cloud modelling, as did Haman (1973), who defined its negative (and called it equivalent specific liquid water content).

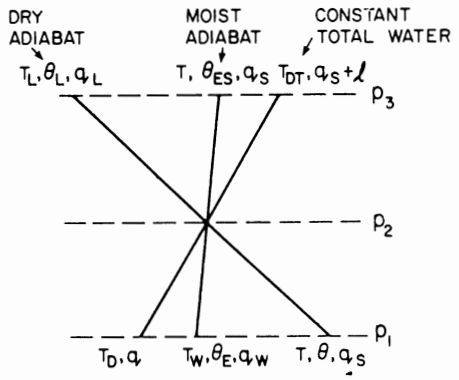

Figure 19. Plot of T, θ, θ_E, q, T_D as they change across a level of saturation to T_L, θ_L, θ_{ES}, $q_s + l$, and T_{DT}.

The wet adiabat is defined by the relation

$$0 = d\theta_{ES}/\theta_{ES} = d\theta/\theta + (L/c_p T)dq_s \quad . \quad . \quad \text{(A1)}$$

where some slight approximation is involved if we keep L and c_p constant. Additionally (Betts 1973b),

$$0 = d\theta_L/\theta_L = d\theta/\theta - (L/c_p T)\,dl \quad . \quad . \quad \text{(A2)}$$

since

$$0 = dq_s + dl. \quad . \quad . \quad . \quad . \quad . \quad \text{(A3)}$$

Consider the change from p_2 to p_1 on Fig. 19.

From Eq. (A1)

$$(T/\theta)\,\delta\theta = (L/c_p)\,\delta q_s \quad . \quad . \quad . \quad \text{(A4)}$$

If we neglect the vertical variation of T/θ, another small approximation for shallow layers, Eq. (A4) becomes, for the level p_1,

$$T - T_W = (L/c_p)(q_W - q), \quad . \quad . \quad . \quad \text{(A5)}$$

confirming that with slight approximation the wet bulb temperature lies on the θ_{ES} wet adiabat through the lifting condensation level p_2. Similarly, above cloud base, from Eq. (A2), we obtain with slight approximation

$$T - T_L = (L/c_p)(q_s + l - q_s) = (L/c_p)\,l \quad . \quad . \quad \text{(A6)}$$

Thus, the meaning of the three temperatures T_D, T, T_L above cloud base is closely akin to T, T_W, T_D, albeit reversed. Considering level p_3, if we started with air at temperature T_L and supersaturated, with total water *vapour* equal to $q_s + l$ corresponding to T_{DT}, this unstable thermodynamic state will move towards saturation at T with condensed liquid water l: i.e. the air would warm T–T_L by condensing $l\,\mathrm{g\,kg^{-1}}$ of vapour. The equivalent interpretation at level p_1 is that if we introduce liquid water to air with properties (T, q) this too is unstable and moves towards saturation at T_W.

The sense in which T_L is physically meaningful becomes clearer if we consider two processes:

(i) The heat, Q, required to raise the temperature of a parcel until it is just saturated (its 'dewpoint') is given by

$$Q = c_p(T_{DT} - T) + Ll = c_p(T_{DT} - T_L) \quad . \quad . \quad \text{(A7)}$$

It is as if we must heat dry air from T_L to T_{DT}.

(ii) In isobaric mixing where evaporation may occur, it is averages of T_L (and θ_{l_1}) that are conserved, since from Eq. (A6)

$$T_L = T - Ll/c_p \quad . \quad . \quad . \quad \text{(A8)}$$

It is clear that if more water condenses or evaporates, T changes accordingly. For example, if we isobarically mix a parcel (T, T_L, p_3) with an equal mass of air at temperature $T = T_L$, but with subsaturation $q_s - q_L + l$, where q_L is the saturation mixing ratio at temperature T_L, then all the liquid water will just evaporate, cooling the first parcel, and the mixture will be just saturated at T_L with water vapour q_L.